Volume 0 (2015), Number 0 pp. 1–12 COMPUTER GRAPHICS *forum*

Robust Cardiac Function Assessment in 4D PC-MRI Data of the Aorta and Pulmonary Artery

Benjamin Köhler[1], Uta Preim[2], Matthias Grothoff[3], Matthias Gutberlet[3], Katharina Fischbach[4], Bernhard Preim[1]

[1] Department of Simulation and Graphics, Otto-von-Guericke University, Magdeburg, Germany
[2] Department of Diagnostic Radiology, Municipal Hospital, Magdeburg, Germany
[3] Department of Diagnostics and Interventional Radiology, Heart Center, Leipzig, Germany
[4] Department of Radiology and Nuclear Medicine, University Hospital, Magdeburg, Germany

ben.koehler@isg.cs.uni-magdeburg.de

Abstract

Four-dimensional phase-contrast magnetic resonance imaging (4D PC-MRI) allows the non-invasive acquisition of time-resolved, three-dimensional blood flow information. Stroke volumes (SVs) and regurgitation fractions (RFs) are two of the main measures to assess the cardiac function and severity of valvular pathologies. The flow rates in forward and backward direction through a plane above the aortic or pulmonary valve are required for their quantification. Unfortunately, the calculations are highly sensitive towards the plane's angulation since orthogonally passing flow is considered. This often leads to physiologically implausible results. In this work, a robust quantification method is introduced to overcome this problem. Collaborating radiologists and cardiologists were carefully observed while estimating SVs and RFs in various healthy volunteer and patient 4D PC-MRI datasets with conventional quantification methods, i.e., using a single plane above the valve that is freely movable along the centerline. By default it is aligned perpendicular to the vessel's centerline, but free angulation (rotation) is possible. This facilitated the automation of their approach which, in turn, allows to derive statistical information about the plane angulation sensitivity. Moreover, the experts expect a continuous decrease of the blood flow volume along the vessel course. Conventional methods are often unable to produce this behavior. Thus, we present a procedure to fit a monotonous function that ensures such physiologically plausible results. In addition, this technique was adapted for the usage in branching vessels such as the pulmonary artery. The performed informal evaluation shows the capability of our method to support diagnosis; a parameter evaluation confirms the robustness. Vortex flow was identified as one of the main causes for quantification uncertainties.

Categories and Subject Descriptors (according to ACM CCS): I.4.9 [Computing Methodologies]: Image Processing and Computer Vision—Applications

1 Introduction

The genesis and evolution of cardiovascular diseases (CVDs) depends on various factors. Recent works have shown that atypical flow patterns such as vortices can be found in many pathologies of the cardiovascular system [FSS*12, HHM*10, KGP*13]. Yet, when it comes to assessing the severity, quantitative measures are essential.

4D phase-contrast magnetic resonance imaging (PC-MRI) allows to gain insight into the patient-specific hemodynamics. Such time-resolved, three-dimensional flow information have a great potential to support diagnosis and the choice of appropriate treatments. Advances in recent years greatly reduced acquisition times and thus increased the viability for clinical routine [HSD13]. However, 4D PC-MRI acquisitions are currently mostly performed for the sole purpose of research. There is a lack of standardized, easy-to-use and (semi-)automatic approaches that increase the practical applicability [MFK*12]. Though, different research groups explore the potential of 4D PC-MRI by developing new and improving existing evaluation methods. In addition, reliability is validated via comparisons to the current 2D PC-MRI standard as well as simulated CFD data.

Two of the most important quantitative measures to assess the cardiac function are *stroke volumes (SV)* and *re-*

gurgitation fractions (RFs). The first describes the volume of pumped blood per heartbeat. Thus, it is the *net flow volume (NFV)*, i.e., the difference between *forward (FFV)* and *backward flow volume (BFV)* above the aortic or pulmonary valve. The second characterizes the *percentaged backward flow volume (PBFV)* into the corresponding ventricle during diastole. Both quantifications require the *flow rates* in forward and backward direction through a plane that is usually aligned orthogonally to the vessel's centerline. Unfortunately, the calculations are highly dependent on the plane's angulation. Unlike 2D PC-MRI, where unsatisfying results make a whole new acquisition necessary, 4D PC-MRI datasets contain the patient's full four-dimensional flow information. This allows to evaluate multiple planes with different positions and angulations *after* the scan.

In this work, various healthy volunteer and patient datasets were analyzed in close collaboration with radiologists and cardiologists. We carefully observed their manual approach to estimate SVs and RFs while anticipating the high sensitivity towards the plane angulation. From this we derived an automatic procedure which systematically analyzes multiple angulations for one position on the vessel's centerline. The obtained statistical information facilitate the robust quantification of the measures and the visualization of uncertainties.

The collaborating experts expect the SV, i.e., the highest NFV, directly above the aortic or pulmonary valve. From there a continuous decrease along the vessel course is assumed due to smaller vessels that branch off and supply blood to certain body regions. However, noise and a low spatio-temporal data resolution often lead to physiologically implausible results, i.e., the NFV development is not monotonous. We employed these two expectations as heuristics to establish a procedure that fits a function which guarantees the desired behavior. In addition, we adapted this method for the use in branching vessels such as the pulmonary artery. Summarizing, the main contributions of this paper are:

- We automated the cardiologists' and radiologists' manual approach to determine net flow and stroke volumes as well as percentaged backward flow volumes and regurgitation fractions despite of the calculations' high sensitivity towards the plane angulation. Derived statistical information are used to illustrate uncertainties. Potential causes are identified in an informal evaluation of selected datasets. This work is an extension of a previous paper [KPG*14].
- We employed the experts' expectations about the net flow volume development along the vessel course to create a procedure that fits a physiologically plausible function.
- We put emphasis on a GPU implementation and thus provide detailed information about required data models.

Section 2 provides basic information about 4D PC-MRI, related quantification and visualization techniques. Section 3 continues with medical background including selected pathologies, data acquisition and preprocessing. Requirements are analyzed in Section 4. Section 5 explains our robust quantification method. We present and discuss results in Section 6 and draw conclusions in Section 7.

2 Related Work

4D PC-MRI: Markl et al. [MFK*12] provide an overview about 4D PC-MRI. Calkoen et al. [CRvdG*14] document its high flexibility by summarizing recent applications. Software solutions were introduced that provide a data preprocessing pipeline [HFS*11]. Temporal maximum intensity projections (TMIPs) are contrast-enhanced images for vessel segmentation [vPBB*10].

Qualitative 4D PC-MRI Data Analysis: Particle animations as well as integral lines enhanced with halos [MTHG03] and illumination [ZSH96] are common flow visualization techniques that can be adapted for the cardiac context. Illustrative [BMGS13] and other expressive visualizations [HGH*10] are used to reduce visual clutter and to enhance the spatial perception. Lawonn et al. [LGP14] address the combined visualization of vessels with internal blood flow. Lens-based focus-and-context visualization [GNBP11] as well as special widgets to probe the flow guided by the vascular anatomy [NJB*11] support the qualitative analysis of the highly complex data. Line predicates were used to extract vortex flow [BPM*13] and the λ_2 criterion was determined as most suitable for the cardiac context [KGP*13]. Noise robustness was improved using an orthogonal decomposition of the flow data [CBW*14].

Quantitative 4D PC-MRI Data Analysis: Stroke volumes help to assess the cardiac function and severity of pathologies [FSS*12, RAFJ*14]. Flow rates are the basis for their quantification. Hoogeveen et al. [HBV99] document errors when they are calculated as flow through a plane, which is the common way in 2D PC-MRI. Thus, they introduced a model-based approach with increased accuracy. Bakker et al. [BHV99] summarized potential sources of errors in 2D PC-MRI acquisitions such as aliasing (phase wraps). Altered wall shear stress is associated with different pathologies. It can be approximated from 4D PC-MRI data although the calculation is highly sensitive towards the spatial resolution [vOPG*13]. Hope et al. [HSD13] provide an overview of further quantitative measures.

3 Medical Background

4D PC-MRI blood flow data help to correlate cardiovascular diseases to different qualitative and quantitative aspects.

3.1 Cardiac Function

During systole, oxygenated blood is pumped from the left ventricle through the aortic valve into the systemic circulation while deoxygenated blood is pumped from the right ventricle through the pulmonary valve into the pulmonary circulation.

Net Flow Volume: Using 4D PC-MRI, net flow volumes (NFVs) can be obtained in an arbitrary vessel section as flow through a plane. A common default is to align the plane or-

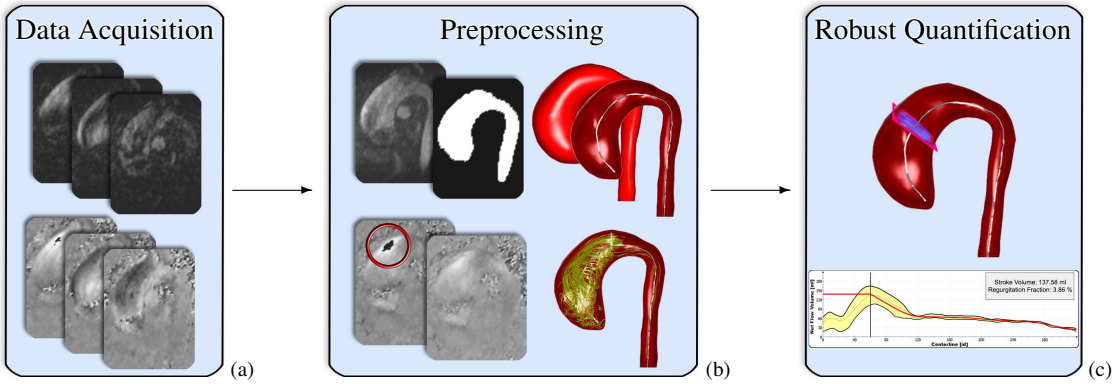

Figure 1: *(a) Each three (xyz) magnitude (top) and phase images (bottom) describe the flow strength and direction, respectively. (b) Top: a 3D segmentation is performed on a temporal maximum intensity projection (TMIP) of the magnitude images and used to extract the vessel mesh including centerline. Bottom: vortex flow is extracted after the phase images were corrected. (c) Our robust method for a junction-free centerline is applied.*

thogonal to the vessel's centerline. However, since only orthogonally passing flow contributes to the NFV, angles between the measurement plane's normal vector and velocity vectors obtained on the plane are critical.

Stroke Volume: The stroke volume (SV) is the amount of pumped blood per heartbeat from either the left or the right ventricle. Therefore, it is the NFV measured directly above the aortic or pulmonary valve. The average of both values over multiple heartbeats should coincide.

Percentaged Backward Flow Volume: If a valve does not close properly during diastole, a percentage of the ejected blood (PBFV) flows back.

Regurgitation Fraction: The regurgitation fraction (RF) is the PBFV into the left or right ventricle. Thus, it is measured directly above the malfunctioning aortic or pulmonary valve. RFs below 5% occur even in healthy persons and are considered as unproblematic [WKS*09].

3.2 Selected Pathologies

Flow in the aorta and pulmonary artery is normally laminar with a parabolic velocity profile. Vortices potentially disturb this pattern which influences the NFV / SV and PBFV / RF calculations. Thus, we explain selected pathologies that promote such complex flow. Natural slight helices can occur in the aortic arch and right pulmonary artery [BPS*13].

Vessel Diameter Alterations: An *ectasia* denominates a vessel dilation up to 1.5 times the original diameter; above they are called *aneurysm*. A *coarctation / stenosis* is a pathologic narrowing. The altered morphology promotes the formation of vortex flow in the corresponding vessel section.

Valve Defects: A healthy aortic valve consists of three leaflets. In *bicuspid aortic valves (BAV)* two of them adhere. The altered BAV's opening characteristics often cause systolic vortex flow in the ascending aorta [HHM*10].

Tetralogy of Fallot: This congenital pathology is characterized by four conditions. It is surgically corrected within months after birth. However, this leads to a progressing *pulmonary insufficiency*. Increased vortex flow was observed in the pulmonary artery and right ventricle [FSS*12].

3.3 Data Acquisition and Preprocessing

A cyclic 4D PC-MRI dataset covers one full heart beat and consists of each three (xyz) time-resolved magnitude and phase images that represent the flow strength and direction, respectively. Our datasets were acquired with a 3 T Magnetom Verio MR (Siemens Healthcare, Erlangen, Germany) with a dedicated 32-channel cardiac coil. An acquisition took about 20 minutes. The echo and repetition time were 3.2 and 6.1 ms, respectively. The sampling bandwidth was 491 Hz/pixel. Prospective echocardiographic (ECG) gating was performed to minimize heart and wall motion artifacts. The V_{ENC} parameter for the maximum expected velocity was set to 1.5 m/s – a common choice for aortic blood flow [MFK*12]. The grid size is 132 rows$\times$192 columns$\times$15–23 slices for each of the 14–21 time steps. The obtained spatial resolution is 1.77 mm$\times$1.77 mm$\times$3.5 mm with about 50 ms difference between subsequent temporal positions. Achieving higher, e.g., isotropic resolutions would significantly increase the acquisition times, which is not feasible for the clinical context. Respiratory control was not carried out for the same reason. Artifacts in the phase images were reduced via eddy current correction [WCS*93] and phase unwrapping [DR04]. Figure 1 illustrates the pipeline.

Vessel Segmentation: A TMIP of the magnitude images represents the maximum flow velocity during the cardiac cycle per voxel. Thus, a corresponding segmentation is a 3D approximation of the dynamic vessel. The normally centrally located main blood flow jet appears prominently, while near-wall regions and vessel sections with greater valve distance may lack contrast. Therefore, the use of a non-automatic segmentation method that allows user corrections seems appropriate. Threshold-based methods such as region growing might not handle the varying contrasts, whereas model-

based methods such as active contours have to compromise between high flexibility in order to capture pathologic vessel shapes and noise robustness. LiveWire [SPP00] would be convenient if one finds a suitable cost function and is willing to process each image slice individually.

We decided to employ a 3D graph cut (GridCut) [BK01, JSH12, LS10]. The only user task is to specify regions in- and outside the vessel, which is intuitive for medical doctors. The amount of required input depends on the TMIP quality. Edge weights between nodes in the graph are set to $\exp(-\alpha \cdot ||\nabla I||^2)$, where $I \in [0,1]$ are the image intensities and the tolerance parameter $\alpha = 1000$ (our default) was experimentally determined. The segmentation is postprocessed with kernel size 3 morphological closing and opening.

Surface and Centerline Reconstruction: Marching cubes (VTK) is performed on the binary segmentation to extract the vessel surface. The subsequent centerline extraction calculates minimum arc length paths that follow local maxima on the distance map which is based on the Voronoi diagram of the surface points [AIR03]. The user specifies a start- and one or multiple endpoints and thus can indirectly exclude undesired vessel branches from the centerline topology. Further parameters are not required. A branch splitting is employed in this work to distinguish between the left and right pulmonary artery [AS04]. A robust implementation of both methods is provided by VMTK [PVS*09]. The centerline is resampled from an interpolating cubic spline (ALGLIB) to guarantee equal distances of 0.5 mm (our default) between successive points. For visualization purposes, a volume-preserving smoothing [TZG96], which was approved for medical surface models [BHP06], as well as decimation [Hop99] is applied to the mesh (VTK).

Flow Field Evaluation: Velocity vectors $\vec{u} \in \mathbb{R}^3$ are composed using the DOPRI5(4) scheme [DP80]. Each of the required samples $\vec{v} \in \mathbb{R}^3$ at the spatio-temporal position $\vec{p} = (\vec{x},t)$, $\vec{x} \in \mathbb{R}^3$ in the flow field $\mathbb{V}$ is calculated via quadrilinear interpolation. The temporally adjacent velocity vectors $\vec{v_{\lfloor t \rfloor}} = \mathbb{V}(\vec{x}, \lfloor t \rfloor)$ and $\vec{v_{\lceil t \rceil}} = \mathbb{V}(\vec{x}, \lceil t \rceil)$ are obtained by hardware-accelerated trilinear interpolation. $\vec{v}$ is their linear interpolation with the weight $t - \lfloor t \rfloor$. Our datasets are small enough to fit into the GPU's memory. Thus, data streaming approaches are not necessary.

4 Requirement Analysis

All necessary interactions should fit to the clinicians' mental model and utilize their in-depth understanding of anatomical shapes including occurring variations, e.g., due to pathologies. Therefore, we have to avoid parameter settings that do not correlate to such medical knowledge and provide reasonable default values for numerical input whenever possible.

The automatic evaluation of different plane angulations should need only a small number of angulation samples in order to limit the computational effort. Thus, an adequate sample distribution is required. The obtained information about the NFV deviation shall be utilized to provide insight into uncertainties.

A proper function has to be determined that represents the expected continuous NFV decrease along the vessel course after a peak value (the SV) above the valve. To ensure that the NFV is properly preserved in case of branching vessels, a comparison and, if necessary, correction of the NFV before and after the junction is required.

To exploit the high computational power of the GPU, algorithm parallelization as well as an appropriate data structure for the measuring planes are required.

5 Robust Cardiac Function Assessment

In the following, we describe the NFV as well as PBFV evaluation with increased robustness for one measuring plane at a specific position on the centerline. Afterwards, we employ this procedure to determine a physiologically plausible NFV development along the vessel course and derive the SV as well as the RF. The last part is about necessary adjustments to facilitate usage in branching vessels.

5.1 Observations

Figure 2 shows the typical situation in a patient dataset with pathologic vortex flow where three slightly different measuring planes produce SVs of 35, 83 and 110 ml. Carefully observing our collaborating cardiologists and radiologists in such unsatisfying situations gave insight into their usual approach. They evaluate multiple measuring planes with slightly different positions as well as angulations and estimate a plausible SV based on their experience. We assume that this value is the mean or median of the samples. We also observed that the problem of uncertain quantification is reduced in healthy volunteer datasets.

5.2 Evaluation of a Single Position on the Centerline

In this section, we present the robust NFV quantification method which is an automation of the observed manual approach. We start with a detailed description of the employed measuring plane model and provide basic information about the NFV calculation. Then, we proceed with the systematic angulation sample generation, summarize our GPU-supported evaluation procedure and apply this principle to the PBFV quantification.

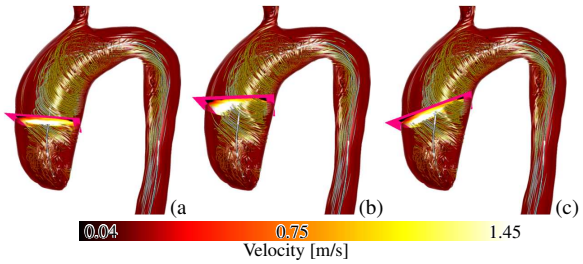

Figure 2: *Slighty different measuring plane configurations produce 35 (a), 83 (b) and 110 ml (c) NFV in this patient with systolic vortex flow in the ectatic ascending aorta.*

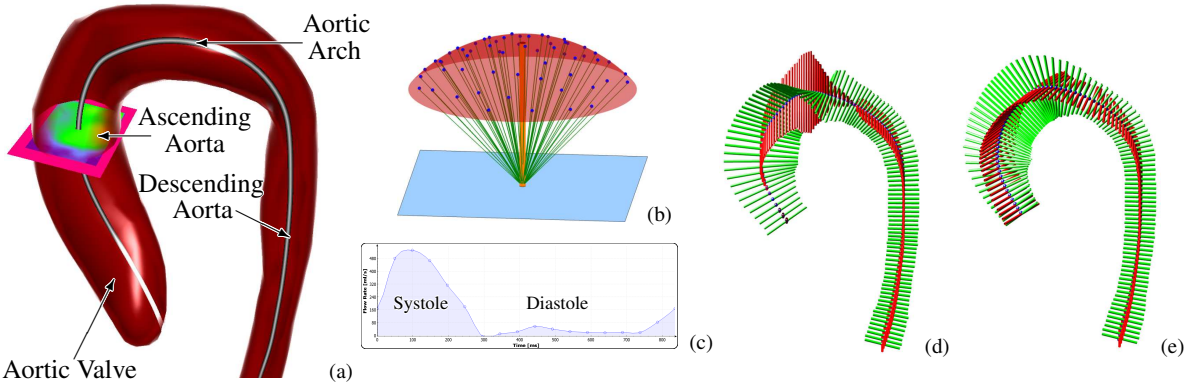

Figure 3: *(a) A measuring plane was fitted to the ascending aorta of this healthy volunteer. (b) Poisson-distributed angulation samples (green) were generated on a $\alpha = \pi/4 \mathrel{\widehat{=}} 45^o$ sphere section (red) around the plane's (blue) normal vector (orange). (c) The net flow volume (NFV) is obtained as integral of the time-dependent flow rate. (d, e) Local coordinate systems of measurement planes orthogonal to the aorta's centerline without (d) and with (e) consistent alignment.*

Plane Model: Hoogeveen et al. [HBV99] focused on small arteries. They made the simplifying model assumptions that a vessel is cylindrical, straight and has a parabolic velocity profile. However, the aorta and pulmonary artery are the largest arteries in the body, curved and the parabolic velocity profile can be disturbed in case of vortex flow. Therefore, their approach might not be suitable for the cardiac context.

We model a measuring plane as grid with the following components: $\vec{g} = (g_x, g_y)^{\mathrm{T}},\ g_{\{x,y\}} \in \mathbb{N}$ is a parameter that describes the number of rectangles in x- and y-dimension, $\vec{s} = (s_x, s_y)^{\mathrm{T}},\ s_{\{x,y\}} \in \mathbb{R}$ is the size per rectangle. $\vec{c} \in \mathbb{R}^3$ is a center position close to or on the vessel's centerline. $\vec{n} \in \mathbb{R}^3$ is the plane's normal vector, i.e., angulation that is commonly set to the corresponding normalized centerline tangent. $\vec{n}_x$ and $\vec{n}_y \in \mathbb{R}^3$ form a local orthonormal system with $\vec{n}$. $\vec{n}_x$ is determined via cross product of $\vec{n}$ with the x-axis $(1,0,0)^{\mathrm{T}}$. If $||\vec{n}_x|| = 0$, the cross product is performed with the y-axis. If the length of $\vec{n}_x$ is still 0, the z-axis is used. $\vec{n}_y$ is obtained as $\vec{n}_x \times \vec{n}$.

These information are sufficient to calculate world coordinates $\vec{w} \in \mathbb{R}^3$ for every grid position (x,y):

$$\vec{w} = \vec{c} + \left(s_x \cdot \vec{n}_x \cdot \left(x - \frac{g_x}{2}\right)\right) + \left(s_y \cdot \vec{n}_y \cdot \left(y - \frac{g_y}{2}\right)\right) \quad (1)$$

The low memory requirements are advantageous for GPU computation.

Fitting a Plane to the Vessel: The size per rectangle $\vec{s} \in \mathbb{R}^2$ has to be determined by fitting the plane P to the vessel. For this purpose, the plane's intersection curve with the triangular vessel mesh is determined. Then, the maximum extents in $\vec{n}_x$ and $\vec{n}_y$ dimension are analyzed and $\vec{s}$ is set accordingly so that P is the minimum axis-aligned bounding rectangle (AABR) of the vessel cross-section. $\vec{c}$ is set to the AABR's center. Figure 3a shows an example of a plane fitted to the ascending aorta.

Basic Net Flow Volume Quantification: The time-dependent flow rate $fr(t)$, $t \in [0, T-1]$, where T is the number of temporal positions in the dataset, is required to calculate the NFV for the plane P:

$$fr(t) = s_x \cdot s_y \cdot \vec{n} \cdot \sum_{x=0}^{g_x-1} \sum_{y=0}^{g_y-1} S\big(P(x,y)\big) \cdot \mathbb{V}\big(P(x,y), t\big)$$

$$\text{with} \quad S\big(P(x,y)\big) = \begin{cases} 1, & P(x,y) \text{ inside vessel} \\ 0, & \text{else} \end{cases} \quad (2)$$

$P(x,y)$ is the grid position (x,y) transformed to world coordinates $\vec{w}$ (see Equation 1). $\mathbb{V}(P(x,y),t)$ are velocity vectors $\vec{u}$ in the flow field $\mathbb{V}$, which is given by the phase images. The product $s_x \cdot s_y$ is the area per rectangular grid element. Since a 4D PC-MRI dataset contains one full heartbeat, $fr(t)$ is periodic. The integral of $fr(t)$ provides the NFV, depicted in Figure 3c. A periodic spline fitting (ALGLIB) is utilized in the implementation. The vessel segmentation is employed to realize $S(P(x,y))$. This allows to exploit hardware-accelerated 3D texture lookups on the GPU.

Plane Angulation Sample Generation: The automatic evaluation of different plane angulation samples $\vec{a}$, i.e., normal vectors requires their systematic generation. All possible angulations form a half sphere, where the plane's original normal vector $\vec{n}$ points to the top. The maximum angle between $\vec{n}$ and $\vec{a}$ is $\alpha = \pi/2 \mathrel{\widehat{=}} 90^{\mathrm{o}}$. Lower α values restrict the angulation to a smaller sphere section. Thus, α describes an angulation tolerance.

The inverse cumulative distribution function (CDF) method allows to generate uniformly distributed samples on a sphere within $[\theta_1, \theta_2]$ and $[\phi_1, \phi_2]$, where θ and ϕ are longitude and latitude, respectively:

$$\theta = \operatorname{acos}\Big(\cos(\theta_1) + u \cdot \big(\cos(\theta_2) - \cos(\theta_1)\big)\Big)$$
$$\phi = \phi_1 + v \cdot (\phi_2 - \phi_1) \quad (3)$$

u and $v \in [0,1]$ are uniformly distributed random numbers. For $\vec{n} = (0,0,1)^{\mathrm{T}}$ the sphere section is described by $\phi_1 = 0$, $\phi_2 = 2\pi$, $\theta_1 = 0$ and $\theta_2 = \alpha \in [0, \pi/2]$. The samples are transformed from spherical coordinates $(1, \theta, \phi)$ to Carte-

Algorithm 1 Robust Net Flow Volume Quantification

```
1:  procedure ROBUST_NFV
2:      P ← measuring plane (Sec. 5.2)
3:      A ← angulation samples
4:      for i ← 0 to size(A)−1 do
5:          /*normal*/ P.n⃗ ← A_i
6:          P.n⃗_x, P.n⃗_y ← orthonormal system construction
7:          /*scale*/ P.s⃗ ← fit P to vessel mesh
8:          GPU buffer ← add parameters of current P
9:      F ← FLOWRATES_GPU() // one thread per angulation
10:     NFV ← net flow volumes
11:     for i ← 0 to size(A)−1 do
12:         f ← time-resolved flow rates F_i for A_i
13:         S ← periodic spline fitted to f
14:         NFV_i ← integral of S (Fig. 3c)
15:     return NFV

1:  procedure FLOWRATES_GPU()
2:      P ← current measuring plane configuration
3:      𝕍 ← flow field
4:      T ← number of temporal positions
5:      fr ← flow rate vector of size T
6:      for x ← 0 to /*grid size x*/ P.g_x−1 do
7:          for y ← 0 to /*grid size y*/ P.g_y−1 do
8:              w⃗ ← (x, y) to world coordinates
9:              if w⃗ in binary vessel segmentation then
10:                 for t ← 0 to T−1 do
11:                     u⃗ ← 𝕍(w⃗, t) (Sec. 3.3)
12:                     fr_t ← fr_t + u⃗ · P.n⃗
13:     for t ← 0 to T−1 do
14:         fr_t ← fr_t · (P.s_x · P.s_y) // area per rectangle in grid
15:     return fr
```

sian coordinates (x,y,z) and used to obtain the angulation sample $\vec{a} = x \cdot \vec{n}_x + y \cdot \vec{n}_y + z \cdot \vec{n}$, where $\vec{n}_x$ and $\vec{n}_y$ are part of the plane's local orthonormal system (LCS).

We generate Poisson-distributed angulations [Jon06] to ensure that the whole sphere section is covered with a small number of samples, which limits computational effort. The parameter $d_{\min}$ describes the minimum distance of two angulations on the unit sphere surface. A new distribution is calculated for each plane evaluation to avoid bias. Figure 3b depicts the angulation samples.

Robust Net Flow Volume Quantification: The NFV determination for one plane is summarized in Algorithm 1. The evaluation of all angulations provides a range of NFVs with an unknown distribution and possible outliers. Thus, the median of these samples is used as robust result.

Robust Percentaged Backward Flow Volume Quantification: The NFV determination is directly applicable for the PBFV quantification. This requires the forward (FFV) and backward flow volume (BFV). They are calculated as integral of the positive and negative part of the flow rate $fr(t)$, i.e., they are the curve's area above and below 0, respectively. For this purpose, line 14 in the ROBUST_NFV procedure of Algorithm 1 is adapted accordingly. Analogous to the NFV, the FFV / BFV distributions' median values are used as result. The PBFV for one position on the centerline is then obtained as $\mathrm{BFV}/(\mathrm{FFV}+\mathrm{BFV})$.

5.3 Evaluation of a Junction-free Centerline

In the following, we explain how to obtain the SV as well as RF and a process to fit a physiologically plausible function to the NFV development along the vessel course. The resulting function represents our collaborators' expectations.

Denoising Plane Sizes: The fitting of planes to the vessel cross-section might produce degenerated sizes if the segmentation contains perpendicularly branching vessels. The scales $\vec{s}$ per rectangular grid element will be too large which negatively affects the NFV quantification. Therefore, we perform a smoothing of scales along the centerline as a preprocessing step. For this purpose, a consistent alignment of the planes' local coordinate systems (LCSs) is required. Unfortunately, if the LCS of each plane is constructed independently using cross products with the x-, y- and z-axis (recall Sec. 5.2) there will be a twist, as shown in Figure 3d. Therefore, only the first plane's LCS $\vec{n}^{\,0}$, $\vec{n}_x^{\,0}$, $\vec{n}_y^{\,0}$ is determined this way. Consistent orientation of $\vec{n}^{\,i}$, $\vec{n}_x^{\,i}$, $\vec{n}_y^{\,i}$, $i>0$ with its predecessor $\vec{n}^{\,i-1}$, $\vec{n}_x^{\,i-1}$, $\vec{n}_y^{\,i-1}$ is achieved by employing the angle θ and rotation axis $\vec{r}^{\,i} = \left(r_x^i,\, r_y^i,\, r_z^i\right)^{\mathrm{T}}$ between $\vec{n}^{\,i}$ and $\vec{n}^{\,i-1}$:

$$\theta = \operatorname{acos}\left(\vec{n}^{\,i} \cdot \vec{n}^{\,i-1}\right) \qquad \vec{r}^{\,i} = \vec{n}^{\,i} \times \vec{n}^{\,i-1} \tag{4}$$

If $||\vec{r}^{\,i} = 0||$, i.e., the normal vectors point in the same direction, then $\vec{n}_x^{\,i} = \vec{n}_x^{\,i-1}$ and $\vec{n}_y^{\,i} = \vec{n}_y^{\,i-1}$. Otherwise, $\vec{n}_x^{\,i} = R \cdot \vec{n}_x^{\,i-1}$ and $\vec{n}_y^{\,i} = R \cdot \vec{n}_y^{\,i-1}$, where R is the general rotation matrix around $\vec{r}^{\,i}$:

$$R = \cos\theta \cdot I + \sin\theta \cdot \begin{bmatrix} 0 & -r_z^i & r_y^i \\ r_z^i & 0 & -r_x^i \\ -r_y^i & r_x^i & 0 \end{bmatrix} + (1-\cos\theta) \cdot \left(\vec{r}^{\,i} \cdot \vec{r}^{\,i\,\mathrm{T}}\right) \tag{5}$$

I is the 3×3 identity matrix. Figure 3e shows $\vec{n}_x$ and $\vec{n}_y$ of the aligned LCS after resampling from a cubic spline (ALGLIB), where the parameter $\rho \in [-15,15]$ controls a non-linearity penalization. $\rho = 2$ is used as default value which, according to the library developers, corresponds to a moderate amount of non-linearity.

Stroke Volume Determination: The robust NFV determination (Algorithm 1) is performed for each of the equidistant centerline points. The x-axis in Figure 4 describes the centerline points in flow direction so that the left part of the plot corresponds to the approximate valve location. The yellow boxes in Figure 4a show the interquartile ranges (IQRs), which are the middle 50% of the sorted NFV samples. Large ranges indicate high sensitivity to the angulation and thus uncertainty in the corresponding vessel section. The thin blue curve interpolates the median NFVs. The SV is ob-

tained as maximum value of this curve. In the following, by NFV and NFV deviations we refer to the median and the IQR of the NFV samples at one centerline position, respectively.

We observed that the IQRs are the most interesting part of the box plots, since outliers, especially behind the valve, may reach unrealistic values such as 10 or 200 ml and thus barely provide further insight. Therefore, we modified the visualization by changing the box plots to a continuous area and removing the whiskers for the minimum and maximum. In addition, this visualization is independent from the centerline length, since no number of box plots needs to be specified. Figure 4a and 4b show a comparison.

The user has the option to limit the evaluation to a part of the centerline in between two specified planes. This can be useful, e.g., if the segmentation contains parts of the ventricles that shall be excluded from the calculation. Additionally, if only the SV and RF are of interest, a restriction to the ascending aorta or pulmonary trunk considerably reduces the computational effort.

Plausible Net Flow Volume Development: Our collaborating cardiologists and radiologists expect a continuous decrease of the NFV after the SV. This is due to smaller vessels that branch off the main vessel and supply blood to certain regions of the body. Yet, even our robust quantification is often not able to produce this behavior. Instead, physiologically implausible local minima and maxima occur. Therefore, we describe a method to enforce this behavior by fitting a monotonous function to the partial NFV function (thin blue curve in Figure 4) right of the SV. In our implementation, this non-trivial task is realized with an iterative cubic, non-linearity penalizing spline fitting (ALGLIB). High and low penalization parameters ρ lead to linear least squares approximation and interpolation, respectively. Our procedure is initialized with $\rho = -5$. After the spline is fitted, its monotonicity is determined by evaluating the signs of all first derivatives. If it is not monotonous, ρ is slightly increased by 0.1, otherwise the loop stops.

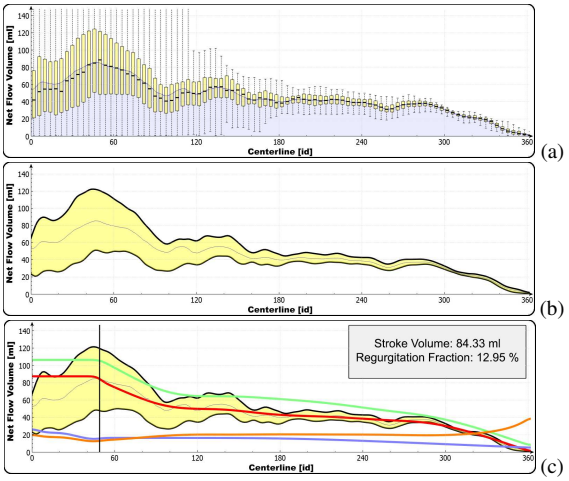

Figure 4: *(a) The net flow volume distributions, obtained with our systematic evaluation of plane angulations for each point of the centerline, are shown as box plots, where the yellow boxes represent the interquartile ranges (IQRs). (b) A modified visualization that is independent from the number of box plots shows the IQR as yellow area graph. (c) The fitted, physiologically plausible functions for the net, forward and backward flow volume are shown in red, green and orange, respectively. The resulting percentaged backward flow volume curve is shown in blue.* 84.33 *ml SV and* 12.95% *RF were determined in this patient with an ectatic ascending aorta. The location is marked by the black vertical line.*

All NFVs between the valve and SV location cannot be lower than the SV and thus are set to the SV as a correction. Unfortunately, C^0 continuity of the fitted monotonous function right and corrected function left of the SV is not guaranteed. As a remedy, both functions are concatenated and smoothed in 15 iterations using a one-dimensional binomial filter with kernel size 5. This is solely performed to increase the visual quality of the diagrams. Therefore, no further parameter analysis is necessary at this point. Figure 4c shows the resulting function in red.

The NFV only decreases due to branching vessels and is constant in vessel sections between two junctions. Following this, the question may arise why no step function is employed as model. This approach would require the locations of all branches and, more critical, a guarantee that all branches are present in the segmentation. The latter is problematic because of limited data resolution and low contrast in smaller vessels due to typically lower flow velocities.

Regurgitation Fraction Determination: The RF is obtained as PBFV at the SV location. If desired, monotonous functions for the FFV, BFV and PBFV can be fitted in the same manner as for the NFV. An example is depicted in Figure 4c. The tasks are independent from one another and thus can be performed in parallel threads on the CPU.

5.4 Evaluation of Bifurcations

In the following, the extension of our method for branching vessels such as the pulmonary artery (PA) is described. The user is required to specify three planes as an initialization. The first one is located at the beginning of the main vessel V_{main}, the second and third are located at the end of the branches B_0 and B_1. Figure 5a shows an example where V_{main} is the pulmonary trunk that splits into the left and right PA which is B_0 and B_1, respectively. A new branching centerline is calculated that starts at the closest point on the vessel surface to the center of the first plane and ends at the corresponding points from the second and third plane. Afterwards, the centerline is split into V_{main}, B_0, B_1 and the junction [AS04] (VMTK). Our method for junction-free centerlines is then applied to each part separately (recall Section 5.3). However, monotonous NFV functions are only fitted for B_0 and B_1. We assume that they are the only branching vessels from V_{main}. In case of the PA this is a fact. Therefore, we set the NFV in V_{main} constant to the SV. Artificial tran-

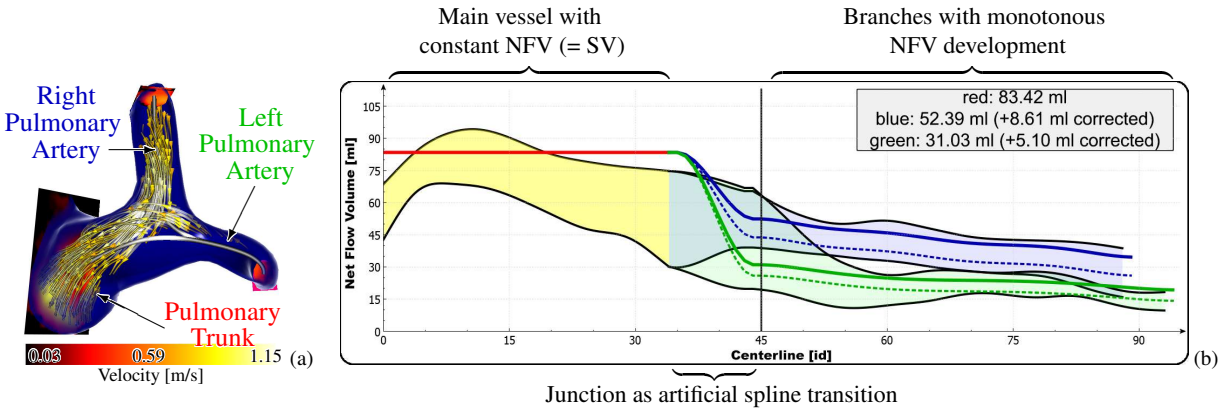

Figure 5: *Plausible net flow volume (NFV) development for branching vessels. (a) High velocity flow during diastole depicts the pulmonary insufficiency of this patient with tetralogy of Fallot. The user is required to specify planes in the main vessel (here: pulmonary trunk (PT)) that splits into two branches (here: left (LPA) and right pulmonary artery (RPA)). (b) The yellow, blue, and green area show the IQRs in the main vessel (PT), first (RPA) and second branch (LPA), respectively. The NFV of the main vessel is set constant to the SV (red line). The blue and green dashed line show the fitted monotonous NFV function for the RPA and LPA, respectively. The black vertical line marks the beginning of the branches. Thus, the junction is between the end of the red and the black vertical line. A NFV correction is performed for each branch to ensure that the sum of the NFVs at the branch beginnings equals the NFV of the main branch (in this case the SV). The results are shown as green and blue solid curve. The RPA NFV was corrected by* 8.61 *ml to a total of* 52.39 *ml and the LPA NFV by* 5.1 *ml to* 31.03 *ml. Their sum equals the* 83.42 *ml that came from the PT.*

sitions that connect the constant NFV / SV from V_{main} with the monotonous NFV curves of B_0 and B_1 in the plot are created using cubic Hermite splines (ALGLIB). They represent the junction. The same is performed for the upper and lower boundaries of the IQR area visualizations.

Based on physiologic considerations, we may assume that the sum of the NFVs at the beginning of the branches ($\text{NFV}(B_0)$ and $\text{NFV}(B_1)$) equals the NFV (SV in case of the PA) from V_{main} ($\text{NFV}(V_{\text{main}})$). Despite using our proposed quantification with increased robustness, this is not always the case. Thus, a correction step is performed:

$$\begin{aligned} \text{NFV}_{\text{diff}} &= \text{NFV}(V_{\text{main}}) - (\text{NFV}(B_0) + \text{NFV}(B_1)) \\ \text{NFV}(B_0) &\stackrel{+}{=} \frac{\text{NFV}_{\text{diff}} \cdot \text{NFV}(B_0)}{\text{NFV}(B_0) + \text{NFV}(B_1)} \\ \text{NFV}(B_1) &\stackrel{+}{=} \frac{\text{NFV}_{\text{diff}} \cdot \text{NFV}(B_1)}{\text{NFV}(B_0) + \text{NFV}(B_1)} \end{aligned} \tag{6}$$

The plot includes both the fitted monotonous NFV functions before and after correction. Additionally, the IQR, which can be considered as uncertainty, of B_0 and B_1 is increased by the values of the corresponding NFV corrections. The upper IQR boundary is increased in case of a positive correction, otherwise the lower IQR boundary is decreased. However, the ratio of $\text{NFV}(B_0)$ and $\text{NFV}(B_1)$ before and after correction is the same. Figure 5b shows an example.

6 Results

This section contains an informal evaluation based on selected datasets and a subsequent discussion that includes a justification of employed default parameters.

6.1 Informal Evaluation

We present six selected, anonymized datasets that were discussed with each two collaborating radiologists and cardiologists. The evaluation was performed informally, i.e., no specific tasks had to be solved. The robust NFV quantification for the whole centerline, SV and RF determination as well as monotonous function fitting took about 30 seconds on average per dataset on a GeForce GTX 680 and Intel i7-3930K. All images were directly captured from our software which is used by our clinical collaborators for research purposes.

Healthy Volunteer: The first dataset shows a healthy volunteer. Figure 6a illustrates the result of our procedure. The highest NFV deviations and thus sensitivity to different plane angulations were detected in the ascending aorta and at the beginning of the aortic arch. Two likely reasons can be identified from the discussion with the experts. On the one hand, there is a physiological helix during systole. Regions with laminar flow seem to be less susceptible. On the other hand, different angulations of planes close to the valve have, from the outset, higher potential to cause deviations since the highest flow rates are present in this vessel section.

The NFVs show a physiologically implausible local minimum at about one third of the centerline, where the aortic arch ends. A possible explanation is a small segmentation error. The vessel diameter in and after the aortic arch is 1.5 cm but decreases to 1.24 cm at the transition. Figure 6c shows the systolic flow and a measuring plane close to the valve, where our method determined 79.96 ml SV. A RF of 0.08% indicates a properly functioning aortic valve.

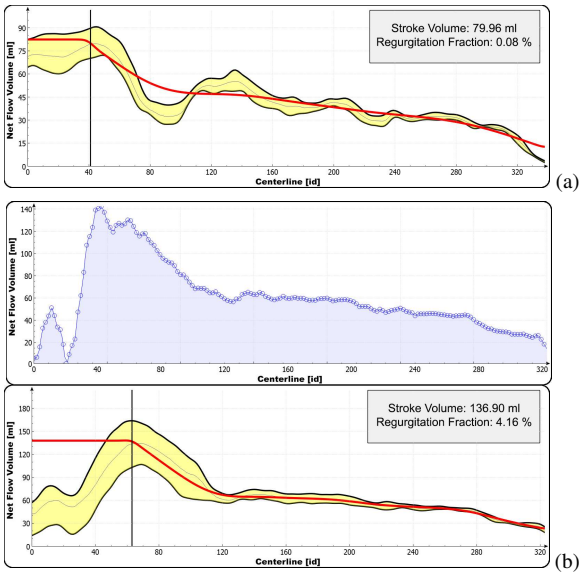

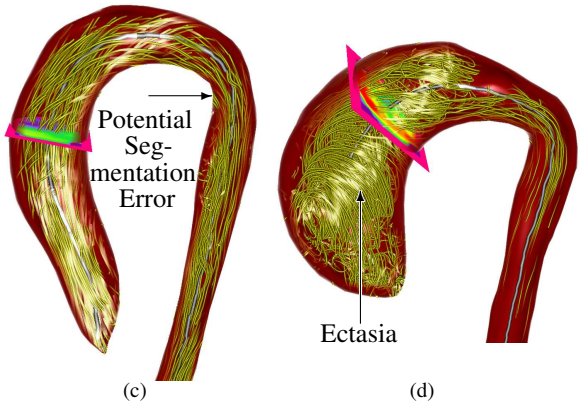

Figure 6: *(a, c) The plane with the SV is located in the ascending aorta of this healthy volunteer. A local NFV minimum at the end of the aortic arch might be due to a potential segmentation inaccuracy. (b, d) A large systolic vortex in the dilated ascending aorta of this BAV patient causes high NFV deviations and a SV that is not located directly above the valve. The upper diagram shows the NFV development when only one perpendicular measuring plane per centerline position is evaluated. Our method (lower diagram) alleviates the problem of quantified NFVs close to 0 ml.*

BAV Patient with Dilated Ascending Aorta: This patient has a bicuspid aortic valve (BAV). The upper diagram in Figure 6b shows the NFVs along the vessel course when one orthogonally aligned measuring plane per centerline position is evaluated. A nearly vanishing value at the beginning is conspicuous. Qualitative flow analysis reveals prominent systolic vortex flow in the abnormally widened ascending aorta. This is likely the cause for the enormous deviations in this vessel section. Our robust NFV procedure alleviates the problem, as shown in the lower diagram of Figure 6b. Figure 6d shows the systolic vortex flow and the location of the plane where 136.9 ml SV were determined. Contrary to the employed heuristic, this is not located directly above the valve but rather at the end of the vortex.

The conventionally quantified RF ranges from 3% to 47%. The experts did agree on an increased amount of retrograde flow, but struggled to specify a concrete value. Our method determined 4.16% RF, which lies within the physiological range.

Figure 4 shows a similar patient with vortex flow in the ectatic ascending aorta. The same high sensitivity to different plane angulations was observed. Figure 7 shows the patient's healthy pulmonary artery. The determined SVs of 80.05 ml and 84.33 ml in the pulmonary artery and aorta, respectively, are physiologically plausible since both values are approximately equal.

Coarctation Patient: The next patient has an aortic coarctation. Qualitative flow analysis shows three systolic vortices: a slight helix above the aortic valve, a small vortex before the narrowing and one large helix in the post-stenotic vessel section, illustrated in Figure 8c. Figure 8a shows the NFV deviations along the centerline. There is a local NFV minimum in the coarctation at about one third of the centerline, which again is considered as physiologically implausible. In addition to potential segmentation inaccuracies like in the healthy volunteer, this might be due to the low data resolution. The vessel diameter shrinks about 50% in the narrowed region. Consequently, it is represented by far less voxels, which enhances partial volume effects.

The highest NFV deviations occur in the post-stenotic vessel section, approximately in the middle of the centerline, directly behind the local maximum. This is where the largest vortex is present. The collaborating experts agree that this is the likely cause for the quantification uncertainties. In contrast to the previous BAV patient, the location of the determined 127.7 ml SV is close to the aortic valve despite of the slight helix.

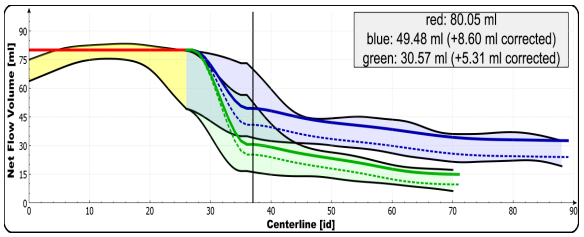

Figure 7: *Healthy pulmonary artery of a patient with dilated ascending aorta (see Figure 4).* 49.48 *ml and* 30.57 *ml of the* 80.05 *ml stroke volume (red) flow into the right (blue) and left pulmonary artery (green), respectively.*

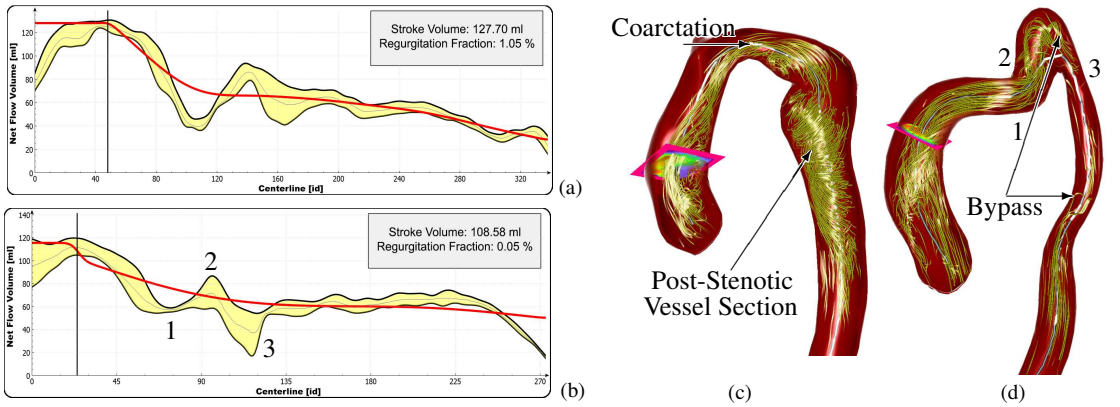

Figure 8: *The SVs in both patients, shown by the planes, were determined close to the valves despite of slight systolic helices. (a, c) A local NFV minimum occurs in the patient's coarctation. The post-stenotic region shows the highest NFV deviations probably due to the large systolic helix. (b, d) Numerous local NFV minima are located in bent vessel sections (1-3) of this patient with a bypass.*

Bypass Patient: An extraanatomic bypass surgery was performed to treat this patient's former coarctation. The altered vessel shape promotes the formation of systolic vortex flow in the ascending aorta, shown in Figure 8d. The obtained diagram is presented in Figure 8b. The SV is located close to the valve despite of the slight helix, like in the previous patient. Moreover, a number of local NFV minima and maxima is noticeable especially at the beginning of the bypass. The numbers 1 to 3 help to connect the diagram with centerline positions. A possible explanation is that partial volume effects make it difficult to capture the quickly changing flow directions in curved vessel sections. However, our monotonous function fitting produces a physiologically plausible NFV development along the centerline.

Tetralogy of Fallot Patient: A surgical correction was performed in this patient with tetralogy of Fallot. The pulmonary insufficiency progressed to a severe state with nearly 25% RF. Figure 5a illustrates the diastolic backward flow in the pulmonary artery. Vortex flow is present in the pulmonary trunk and right pulmonary artery during systole as well as diastole. Our robust quantification for bifurcations, shown in Figure 5b, determined 83.42 ml SV that splits into 52.39 ml and 31.03 ml for the right and left pulmonary artery, respectively. This is physiologically plausible since the right half of the lung consists of three lobes, whereas the left half of the lung with two lobes is smaller due to the neighboring heart.

6.2 Discussion

The user's responsibility is to generate a valid segmentation and centerline. For bifurcations, three planes are required which are located in the origin and the two branches. Reasonable default values for other parameters are investigated at the end of this section.

The sensitivity to different plane angulations was visualized as area graphs that represent the middle 50% (interquartile range, IQR) of box plots. Especially prominent vortex flow seems to cause high uncertainties since corresponding vessel sections show large IQRs. High variations led to careful result interpretations, whereas small deviations created trust.

Contrary to the assumptions, the SVs were not always determined directly above the valve. This is a serious error potential for the common 2D PC-MRI standard in addition to the plane angulation that is required before the acquisition. Though, the automatically obtained SVs show good correspondence with the expected results estimated by our collaborating experts using conventional methods. The SVs are expected between the aortic or pulmonary valve and the location where the first vessel branches off. In the pulmonary artery this is the junction where it splits into left and right. In the aorta, the small coronary arteries close behind the valve are neglected since they receive only a marginal amount of blood (about 5%). Thus, the location is shortly after the beginning of the aortic arch, where the brachiocephalic artery is located. If solely the SV or RF is of interest, a priori knowledge can speed up our robust quantification method by restricting the calculations to the corresponding vessel sections. The user can specify two planes as start and end position for this purpose.

We described a method to analyze bifurcations. The algorithmic adaption to three or more branches is simple. Yet, the resulting plot visualization may become cluttered if two or more branches receive approximately the same volume of blood. In this case, the subgraphs, especially the IQR areas, would overlap. Fortunately, this problem is of minor relevance for the pulmonary artery since the right pulmonary artery normally receives more blood due to the larger right half of the lung.

Sample Generation Parameter Evaluation: Reasonable default values increase the practical applicability of our method. We experimentally determined an appropriate standard configuration during the development process, which is a grid size of $\vec{g} = 50 \times 50$, an angulation tolerance $\alpha =$

$\pi/4 \mathrel{\widehat{=}} 45^o$ and Poisson-distributed angulation samples with a minimum distance of $d_{\min} = 0.075$ on the unit sphere surface (recall Section 5.2). The validation of these parameters is shown exemplary for the SV determination in the BAV patient (recall Section 6.1), which represents our experiences for all datasets.

New angulation samples are generated for each plane evaluation. Thus, every SV analysis is repeated 100 times per parameter set. The defaults produce 136.9 ± 0.87 ml, which is the samples' mean plus minus the standard deviation (std).

Modifications of α produced 146.48 ± 1.27 ml for 15^o, 143.24 ± 1.35 ml for 30^o, 136.9 ± 0.87 ml for the default 45^o, 136.61 ± 0.87 ml for 60^o, 150.64 ± 1.18 ml for 75^o and 163.48 ± 1.1 ml for 90^o. The stds were lowest for 45^o and 60^o and the best agreement with 140 ml SV estimated by the experts was achieved with $\alpha \in [30^o, 60^o]$. As a consequence, $\alpha = \pi/4 = 45^o$, the middle of this range, seems appropriate as default value.

Altered grid sizes produced 130.08 ± 0.53 ml for 5×5, 136.75 ± 1.52 ml for 25×25, 136.9 ± 0.87 ml for the default 50×50, 136.66 ± 0.36 ml for 75×75 and 135.47 ± 0.92 ml for 100×100. There were no significant changes above grid sizes of 25×25. Though, planes that are fitted to large aneurysms with, e.g., 55 mm vessel diameter have isotropic rectangle sizes of $55/25 = 2.2$ mm in 25×25 grids. To ensure that the rectangles are smaller than our data's finest resolution of 1.77 mm in one dimension, we use 50×50 grids as default.

Altered $d_{\min}$ of the Poisson distribution produce 138.73 ± 2.84 ml for 0.165 ($\approx$50 samples), 136.65 ± 1.51 ml for 0.1 ($\approx$125 samples), 136.9 ± 0.87 ml for the default 0.075 ($\approx$200 samples) and 135.76 ± 0.64 ml for 0.05 ($\approx$500 samples). Standard uniform distribution (recall Section 5.2) yields 140.19 ± 10.81 ml for 50 samples, 137.35 ± 6.38 ml for 125 samples, 137.66 ± 5.32 ml for 200 samples and 135.06 ± 3.18 ml for 500 samples. The stds from Poisson distribution are significantly lower than from uniform distribution. It was below 1 ml for $d_{\min} = 0.075$ and reduced only marginally with more samples. The difference between both distributions decreases with an increasing number of samples. However, Poisson distribution requires fewer samples to achieve sufficient results. The higher costs for angulation generation are not substantial. Summarizing, the sample distribution has the highest influence on the results.

7 Conclusion and Future Work

We presented a method to robustly determine net flow (NFV) and stroke volumes (SV) as well as percentaged backward flow volumes (PBFV) and regurgitation fractions (RF) in cardiac 4D PC-MRI data of the aorta and pulmonary artery. The procedure was developed in close collaboration with cardiologists and radiologists and represents an automation of their manual approach. Statistical information and uncertainties were presented as area graphs which were derived from common box plots. The experts' expectations were employed as heuristics to establish a procedure that creates physiologically plausible NFV developments along the vessel course. The GPU's computing power was exploited to achieve average calculation times of 30 seconds.

In addition to segmentation inaccuracies and partial volume effects, prominent vortex flow was identified as main cause for uncertainties. Against the assumption, the SV was not in all cases obtained directly above the aortic or pulmonary valve. This is a source of potential errors for the current 2D PC-MRI standard since the default is to use a plane above the valve that is orthogonal to the vessel's centerline. The robust determination of PBFVs and RFs is of particular importance for the discussion of appropriate treatments. The monotonous function fitting for both junction-free and branching vessels was able to generate physiologically plausible NFV developments.

Due to reasonable default parameters the only required user input is a vessel segmentation and centerline, which both exploit expert knowledge. Hence, our procedure is eligible to be part of an automatic data evaluation procedure in the future that supports clinical report generation. Branching vessels additionally need a specification of the main vessels as well as the branches by placing planes inside each vessel section.

Until now, SV and RF quantification requires knowledge of highly specialized experts on the cardiovascular system and its hemodynamics. Our method reduces this to mainly anatomical knowledge. However, the newly enabled uncertainty assessment still needs experience. More sophisticated visualizations might support the interpretation in the future.

References

[AIR03] ANTIGA L., IORDACHE E. B., REMUZZI A.: Computational Geometry for Patient-Specific Reconstruction and Meshing of Blood Vessels from MR and CT Angiography. *IEEE Trans Med Imag 22*, 5 (2003), 674–84. 4

[AS04] ANTIGA L., STEINMAN D. A.: Robust and Objective Decomposition and Mapping of Bifurcating Vessels. *IEEE Trans Med Imag 23*, 6 (2004), 704–13. 4, 7

[BHP06] BADE R., HAASE J., PREIM B.: Comparison of Fundamental Mesh Smoothing Algorithms for Medical Surface Models. In *Simulation und Visualisierung* (2006), pp. 289–304. 4

[BHV99] BAKKER C. J., HOOGEVEEN R. M., VIERGEVER M. A.: Construction of a Protocol for Measuring Blood Flow by Two-Dimensional Phase-Contrast MRA. *J Magn Reson Imag 9*, 1 (1999), 119–27. 2

[BK01] BOYKOV Y., KOLMOGOROV V.: An Experimental Comparison of Min-Cut/Max-Flow Algorithms for Energy Minimization in Vision. *IEEE Trans Patt Anal Mach Intell 26* (2001), 359–74. 4

[BMGS13] BORN S., MARKL M., GUTBERLET M., SCHEUERMANN G.: Illustrative Visualization of Cardiac and Aortic Blood Flow from 4D MRI Data. In *Proc IEEE PacificVis* (2013), pp. 129–36. 2

[BPM*13] BORN S., PFEIFLE M., MARKL M., GUTBERLET M., SCHEUERMANN G.: Visual Analysis of Cardiac 4D MRI Blood Flow Using Line Predicates. *IEEE Trans Vis Comput Graph 19* (2013), 900–12. 2

[BPS*13] BÄCHLER P., PINOCHET N., SOTELO J., CRELIER G., IRARRAZAVAL P., TEJOS C., URIBE S.: Assessment of

Normal Flow Patterns in the Pulmonary Circulation by Using 4D Magnetic Resonance Velocity Mapping. *J Magn Reson Imag 31*, 2 (2013), 178–88. 3

[CBW*14] CARNECKY R., BRUNNER T. BORN S., WASER J., HEINE C., PEIKERT R.: Vortex Detection in 4D MRI Data: Using the Proper Orthogonal Decomposition for Improved Noise-Robustness. In *Proc EuroVis Short Papers* (2014), pp. 127–31. 2

[CRvdG*14] CALKOEN E. E., ROEST A. A., VAN DER GEEST R. J., DE ROOS A., WESTENBERG J. J.: Cardiovascular Function and Flow by 4-Dimensional Magnetic Resonance Imaging Techniques: New Applications. *J Thorac Imag 29*, 3 (2014), 185–96. 2

[DP80] DORMAND J. R., PRINCE P. J.: A Family of Embedded Runge-Kutta Formulae. *J Comput Appl Math 6*, 1 (1980), 19–26. 4

[DR04] DÌAZ C., ROBLES L. A.: Fast Noncontinuous Path Phase-Unwrapping Algorithm Based on Gradients and Mask. In *Proc Iberoameric Cong Patt Recog* (2004), pp. 116–23. 3

[FSS*12] FRANCOIS C., SRINIVASAN S., SCHIEBLER M., REEDER S., NIESPODZANY E., LANDGRAF B., WIEBEN O., FRYDRYCHOWICZ A.: 4D Cardiovascular Magnetic Resonance Velocity Mapping of Alterations of Right Heart Flow Patterns and Main Pulmonary Artery Hemodynamics in Tetralogy of Fallot. *J Cardiovasc Magn Reson 14*, 1 (2012), 16. 1, 2, 3

[GNBP11] GASTEIGER R., NEUGEBAUER M., BEUING O., PREIM B.: The FLOWLENS: A Focus-and-Context Visualization Approach for Exploration of Blood Flow in Cerebral Aneurysms. *IEEE Trans Vis Comput Graph 17*, 12 (2011), 2183–92. 2

[HBV99] HOOGEVEEN R. M., BAKKER C. J., VIERGEVER M. A.: MR Phase-Contrast Flow Measurement with Limited Spatial Resolution in Small Vessels: Value of Model-based Image Analysis. *J Magn Reson Med 41*, 3 (1999), 520–8. 2, 5

[HFS*11] HENNEMUTH A., FRIMAN O., SCHUMANN C., BOCK J., DREXL J., HUELLEBRAND M., MARKL M., PEITGEN H.-O.: Fast Interactive Exploration of 4D MRI Flow Data. In *Proc SPIE Med Imag* (2011), pp. 79640E–11. 2

[HGH*10] HUMMEL M., GARTH C., HAMANN B., HAGEN H., JOY K.: IRIS: Illustrative Rendering for Integral Surfaces. *IEEE Trans Vis Comput Graph 16*, 6 (2010), 1319–28. 2

[HHM*10] HOPE M. D., HOPE T. A., MEADOWS A. K., ORDOVAS K. G., URBANIA T. H., ALLEY M. T., HIGGINS C. B.: Bicuspid Aortic Valve: Four-Dimensional MR Evaluation of Ascending Aortic Systolic Flow Patterns. *Radiology 255*, 1 (2010), 53–61. 1, 3

[Hop99] HOPPE H.: New Quadric Metric for Simplifying Meshes with Appearance Attributes. In *Proc IEEE Vis* (1999), pp. 59–66. 4

[HSD13] HOPE M. D., SEDLIC T., DYVERFELDT P.: Cardiothoracic Magnetic Resonance Flow Imaging. *J Thorac Imaging 28*, 4 (2013), 217–30. 1, 2

[Jon06] JONES T. R.: Efficient Generation of Poisson-Disk Sampling Patterns. *J Graph Tools 11*, 2 (2006), 27–36. 6

[JSH12] JAMRIŠKA O., SÝKORA D., HORNUNG A.: Cache-Efficient Graph Cuts on Structured Grids. In *Proc IEEE Comput Vis Patt Recog* (2012), pp. 3673–80. 4

[KGP*13] KÖHLER B., GASTEIGER R., PREIM U., THEISEL H., GUTBERLET M., PREIM B.: Semi-Automatic Vortex Extraction in 4D PC-MRI Cardiac Blood Flow Data Using Line Predicates. *IEEE Trans Vis Comput Graph 19*, 12 (2013), 2773–82. 1, 2

[KPG*14] KÖHLER B., PREIM U., GUTBERLET M., FISCHBACH K., PREIM B.: Robust Cardiac Function Assessment in 4D PC-MRI Data. In *Proc Eurographics Vis Comput Biol Med* (2014), pp. 1–10. 2

[LGP14] LAWONN K., GASTEIGER R., PREIM B.: Adaptive Surface Visualization of Vessels With Animated Blood Flow. *Comp Graph Forum 33*, 8 (2014), 16–27. 2

[LS10] LIU J., SUN J.: Parallel Graph-Cuts by Adaptive Bottom-Up Merging. In *Proc IEEE Comput Vis Patt Recog* (2010), pp. 2181–8. 4

[MFK*12] MARKL M., FRYDRYCHOWICZ A., KOZERKE S., HOPE M. D., WIEBEN O.: 4D Flow MRI. *J Magn Reson Imag 36*, 5 (2012), 1015–36. 1, 2, 3

[MTHG03] MATTAUSCH O., THEUSSL T., HAUSER H., GRÖLLER M. E.: *Strategies for Interactive Exploration of 3D Flow Using Evenly-Spaced Illuminated Streamlines*. Tech. rep., Institute of Computer Graphics and Algorithms, Vienna University of Technology, 2003. 2

[NJB*11] NEUGEBAUER M., JANIGA G., BEUING O., SKALEJ M., PREIM B.: Anatomy-Guided Multi-Level Exploration of Blood Flow in Cerebral Aneurysms. *Comp Graph Forum 30*, 3 (2011), 1041–50. 2

[PVS*09] PICCINELLI M., VENEZIANI A., STEINMAN D. A., REMUZZI A., ANTIGA L.: A Framework for Geometric Analysis of Vascular Structures: Application to Cerebral Aneurysms. *IEEE Trans Med Imag 28*, 8 (2009), 1141–55. 4

[RAFJ*14] ROLDÁN-ALZATE A., FRYDRYCHOWICZ A., JOHNSON K. M., KELLIHAN H., CHESLER N. C., WIEBEN O., FRANCOIS C. J.: Non-invasive Assessment of Cardiac Function and Pulmonary Vascular Resistance in an Canine Model of Acute Thromboembolic Pulmonary Hypertension Using 4D Flow Cardiovascular Magnetic Resonance. *J Cardiovasc Magn Reson 16*, 1 (2014), 23. 2

[SPP00] SCHENK A., PRAUSE G., PEITGEN H.-O.: Efficient Semiautomatic Segmentation of 3D Objects in Medical Images. In *Proc MICCAI* (2000), pp. 186–95. 4

[TZG96] TAUBIN G., ZHANG T., GOLUB G.: Optimal Surface Smoothing as Filter Design. In *Proc Europ Conf Comput Vis*. 1996, pp. 283–92. 4

[vOPG*13] VAN OOIJ P., POTTERS W. V., GUÉDON A., SCHNEIDERS J. J., MARQUERING H. A., MAJOIE C. B., VANBAVEL E., NEDERVEEN A. J.: Wall Shear Stress Estimated with Phase Contrast MRI in an In Vitro and In Vivo Intracranial Aneurysm. *J Magn Reson Imag 38*, 4 (2013), 876–84. 2

[vPBB*10] VAN PELT R., BESCOS J. O., BREEUWER M., RACHEL E. C., GRÖLLER M. E., TER HAAR ROMENIJ B., VILANOVA A.: Exploration of 4D MRI Blood Flow Using Stylistic Visualization. *IEEE Trans Vis Comput Graph 16*, 6 (2010), 1339–47. 2

[WCS*93] WALKER P. G., CRANNEY G. B., SCHEIDEGGER M. B., WASELESKI G., POHOST G. M., YOGANATHAN A. P.: Semiautomated Method for Noise Reduction and Background Phase Error Correction in MR Phase Velocity Data. *J Magn Reson Imag 3*, 3 (1993), 521–30. 3

[WKS*09] WÖHRLE J., KOCHS M., SPIESS J., NUSSER T., HOMBACH V., MERKLE N.: Impact of Percutaneous Device Implantation for Closure of Patent Foramen Ovale on Valve Insufficiencies. *Circulation 119*, 23 (2009), 3002–8. 3

[ZSH96] ZÖCKLER M., STALLING D., HEGE H.-C.: Interactive Visualization of 3D-Vector Fields Using Illuminated Streamlines. In *Proc IEEE Vis* (1996), pp. 107–13. 2